Plasma Collision in a Gas Atmosphere

S. Le Pape,[1,4] L. Divol,[1] G. Huser,[2] J. Katz,[3] A. Kemp,[1] J. S. Ross,[1] R. Wallace,[1] and S. Wilks[1]

[1]*Lawrence Livermore National Laboratory, Livermore, California 94550, USA*
[2]*CEA, DAM, DIF, Bruyeres-le-Chatel, F-91297 Arpajon, France*
[3]*Laboratory for Laser Energetics, University of Rochester, 250 East River Road, Rochester, New York 14623, USA*
[4]*LULI-CNRS École Polytechnique, CEA, Université Paris-Saclay, UPMC Univ Paris 06,*
Sorbonne Universités, F-91128 Palaiseau cedex, France

We present a study on the impact of a gas atmosphere on the collision of two counterpropagating plasmas (gold and carbon). Imaging optical Thomson scattering data of the plasma collision with and without helium in between have been obtained at the Omega laser facility. Without gas, we observed large scale mixing of colliding gold and carbon ions. Once ambient helium is added, the two plasmas remain separated. The difference in ionic temperature is consistent with a reduction of the maximum Mach number of the flow from $M = 7$ to $M = 4$. It results in a reduction of a factor ~ 10 of the counterstreaming ion-ion mean free path. By adding a low-density ambient gas, it is possible to control the collision of two high-velocity counterstreaming plasma, transitioning from an interpenetrating regime to a regime in agreement with a hydrodynamic description.

Plasma collisions can have very different characteristics depending on conditions. At low-density, a plasma collision can lead to the formation of collisionless shocks [1,2] that are thought to be the source of magnetic fields and particle acceleration to cosmic ray energies. At higher density, it can lead to the formation of a hot dense plasma used to generate x-ray lasers [3,4]. Colliding plasma are also a key feature in inertial fusion chambers, where the chamber walls are exposed to extreme flux, expected to generate stagnation of plasma clouds that could limit the lifetime of inertial fusion chambers [5,6]. In inertial confinement fusion (ICF), a low-Z capsule containing the DT fuel, is ablatively driven by x ray emanating from the interaction of a high-Z cylinder (hohlraum) and a high-energy laser. The ablated hohlraum wall can collide with the expanding plasma from the compressed capsule [7]. Controlling this collision is important for sustaining laser ignition pulses.

Previous studies of high-velocity plasma collisions in vacuum have shown ballistic or diffusive interpenetration [8,9]. The mixing of the counterstreaming plasma species was only limited by the size of the system or by electrostatic or magnetic instabilities [2,10]. On the other hand, the backpressure provided by a high-density ambient gas can slow down the expansion of a laser driven plasma, allowing control of stagnation in ICF systems, but restricting the laser propagation and coupling to the target [11,12]. In addition, proton radiography of the gas interface has shown a wide mixing layer attributed to Rayleigh-Taylor (RT) instabilities growth seeded by nonuniformity in laser illumination as the expanding plasma slows down in the gas [13].

In this Letter, we report on the successful control of plasma expansions and stagnation by using a low-density or low-Z ambient gas. Imaging Thomson scattering (TS) is used to fully characterize the collision of laser driven gold and carbon plasmas. In the vacuum case, we observe mixing of the ions over the entire field of view, along with strong ion heating, consistent with previous studies [8]. When an ambient helium density of 0.15 mg/cm³ ($n_e = 0.003\%$ of the laser critical density) is added, the carbon and gold ions remains separated with an interface mix width <50 μm (instrumental resolution of the TS diagnostic) and much less ion heating. At this low density, the helium plasma does not provide much backpressure that could lead to RT instabilities (as it is measured to diffuse through the gold and carbon plasmas), but limits the electrostatic potential and acceleration of the front of the plasma expansions. Paradoxically, the presence of a kinetic agent (a low-density helium plasma) keeps the system amenable to a hydrodynamic description. This regime, where the helium gas does not alter the laser beam propagation, is the regime of choice for current attempts at controlling ICF implosions at the National Ignition Facility (NIF).

An experiment was carried out at the Omega laser facility [14] to measure the plasma conditions using optical Thomson scattering. The target [Fig. 1(a)] is composed of a gold band, 1.6 mm in radius, 800 μm in length, and 25 μm thick, and a high-density carbon (HDC) puck ($\rho = 3.45$ g/cm³), 600 μm in radius and 800 μm in length, positioned at the gold band center. To study the impact of helium on the plasma collision, the target is placed inside a
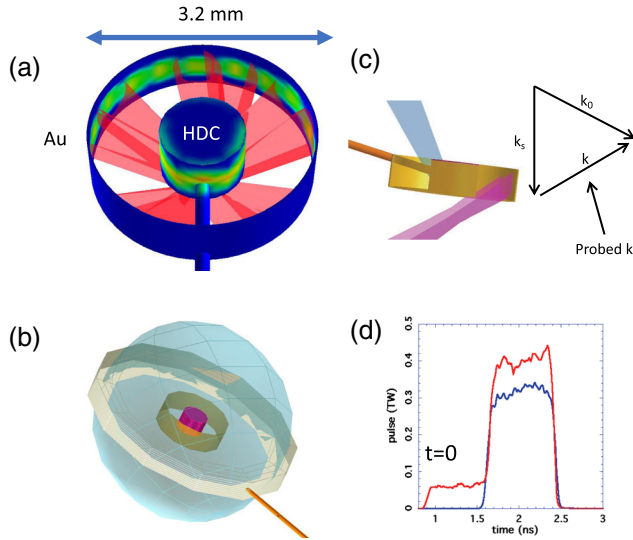
FIG. 1. (a) Schematic of the target for the gold-carbon case. On the target surfaces, the laser intensity is shown as calculated by a 3D thermal radiation and computer aided design code (VISRAD [16]); only a subset of laser beams are shown for clarity. (b) Schematic of the gasbag target. (c) Geometry of the Thomson probe. (d) Laser pulse shape used (blue) without and (red) with the helium gasbag.
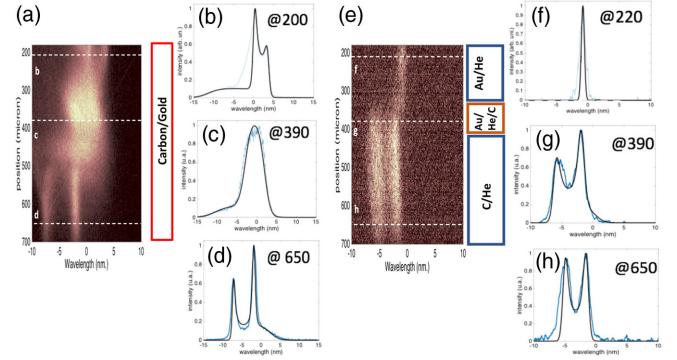

FIG. 2. (a) Spatially resolved Thomson scattering spectra in the gold-carbon case. (b)–(d) (Blue curves) Lineouts over Fig. 2(a) at various positions along the spatial axis. Distances are measured from the Au surface. (Black curve) Theoretical fits to experimental data. (e) Spatially resolved Thomson scattering spectra in the gold-helium-carbon case. (f)–(h) (Blue curves) Lineouts over Fig. 2(e) at various positions along the spatial axis. Distances are measured from the Au surface. (Black curve) Theoretical fits to experimental data.

gasbag filled with 0.15 mg/cm^3 of He4. A gasbag consists of an aluminum washer of inner diameter 4 mm with a thin polyimide (C22H10N2O4) skin bonded to each end. When inflated, a gasbag forms an oblate ellipsoid ~5.5 mm long, with a skin thickness of 0.35–0.4 μm [Fig. 1(b)]. Omega laser beams are focused on the gold and HDC surfaces using phase plates resulting in a 300-μm focal spot. Nineteen laser beans at $\lambda_{3\omega} = 351$ nm were focused on the inside of the gold surface, and nine beams were focused on the surface of the HDC puck. The beam pointing was optimized to reduce intensity variation on the target surface, preventing the apparition of pronounced jets emanating from the space between two clusters of laser spots [15].

For the vacuum shot, i.e., no gasbag, each beam had 300 J in a 1-ns flat top pulse [Fig. 1(d)], leading to an intensity on the target surfaces of 4×10^{14} W/cm^2. When a gasbag was used, each beam had 370 J in a stepped pulse with 300 J in a 1-ns flat top pulse [Fig. 1(d)]. The Thomson scattering diagnostic [17–20] consisted of a 40-J,1-ns-long $\lambda_{4\omega} = 263.23$-nm probe beam with a best-focus diameter of ~50 μm [21]. The intensity of the probe beam, reached at its best focus, is low enough to stay below the filamentation figure of merit defined in [22] in our plasma (1 keV electron temperature at 4ω) and focusing conditions ($f_{number} = 10$).

The light scattered from a $50 \times 50 \times 1000$-μm volume was imaged through a 1/3-m spectrometer. Spatially resolved Thomson scattering measurements are made by aligning the image of the probe beam parallel to the spectrometer input slit (100-μm wide) and recording the spectrally dispersed image on a CCD. The spectral dispersion was 0.411 nm/pixel, and the scattering angle

was 60 deg [Fig. 1(c)]. The Thomson scattering data are taken at the end on the main laser pulse [Fig. 1(d)] for a ~300-ps duration.

Spatially resolved TS spectra are shown in Fig. 2(a) for the gold-carbon case and in Fig. 2(e) for the gold-helium-carbon case. Figures 2(b)–2(d) and 2(f)–2(h) show spectral lineouts for the two cases. The flow velocity can be measured from the Doppler shift of the midpoint of the Thomson scattered signal. The velocities of the carbon and gold flow have opposite directions [23] [Fig. 4(b)], leading to red- or blueshifted spectra. The wavelength separation of the two ionic peaks is related to the sound speed, which is proportional to $\sqrt{[(ZT_e + 3T_i)/M_i]}$, where T_e is the electron temperature, T_i is the ion temperature, M_i is the ion mass, and Z is the ionization state. Here we assumed fully ionized carbon $Z = 6$ and $Z = 45$ [24] for gold, and the ionic peak separation allows the determination of the electron temperature (T_e) when T_i/ZT_e is small. Ionic Landau damping [25,26], when T_i/ZT_e is sizable, broadens the ionic peak, enabling the determination of the ion temperature. Throughout this Letter, the TS spectra are fitted using a multispecies, multiflow kinetic model for the plasma dispersion, which usually allows a determination of the temperature and average flow velocity for each species [27]. The TS power is expressed by using the spectral density function $S = S_e + S_i$ with two ion species j:

$$S_i(k,\omega) = (2\pi/k)|\chi_e(\omega - k.v_e)/\varepsilon|^2$$
$$\times \sum_j (Z_j^2 n_j/n_e) f_{j0}((\omega - k.v_j)/k)),$$

where $\omega = \omega_s - \omega_0$, ω_s and ω_0 are the frequency of the scattered light and TS probe, respectively, n_j is the density of each ion species, v_j is the drift velocity in the

laboratory frame, ε is the dielectric function and χ_e the electron susceptibility, f_{j0} is the ion velocity distribution function and Z_j is the average charge state.

Similarly, $S_e(k,\omega) = (2\pi/k)|1 + \sum_j(\chi_j(\omega - k.v_j)|^2 / \varepsilon^2 f_{e0}((\omega - k.v_e)/k))$, where $n_e v_e = \sum_j(n_j Z_j v_j)$ to insure zero net current. Finally, $\varepsilon(k,\omega) = 1 + \chi_e(\omega - k.v_e) + \sum_j(\chi_j(\omega - k.v_j))$ where χ_j are the ion susceptibilities. All particle distribution functions are assumed Maxwellian. An additional electron drift can be added to match further details in the asymmetry of the ion acoustic peaks.

In the vacuum case, the entire plasma at the time of the measurement is a hot mix of gold and carbon ions, the two counterstreaming plasmas having interpenetrated [Fig. 2(a)]. When a low-density (0.15 mg/cm^3) ambient helium gas is added, a narrow (~ 50 μm) cold mix layer separates the gold plasma from the carbon plasma [Fig. 2(e)], with the He ions diffusing across the boundary. From the lineouts in Fig. 2, more detailed data on the plasma conditions can be extracted. At the 200-μm position near the gold wall [Figs. 2(b) and 2(f)], ion gold peaks are observed in both cases. In the gold-carbon case, a blue-shifted tail and an asymmetry of the ionic peak can be observed, indicative of fast carbon ions having reached this position. In the gold-helium-carbon case, only one gold peak is observed. In the gold plasma [Figs. 2(d) and 2(f)] the symmetry of the ion peaks is affected by Landau damping induced by light ions mixing (helium or carbon). The blueshifted peak is totally suppressed in the gold-helium case. At the 400-μm position [Figs. 2(c) and 2(g)], the gold-carbon case shows a broad single peak, while the gold-helium-carbon case shows two separated carbon peaks. The broad ionic peak observed is due to the presence of hot (>20 keV) gold and carbon ions in the same region. The two asymmetric carbon ion peaks observed are due to the presence of cold (<1 keV) carbon mixed with cold (<1 keV) helium ions. At the 650-μm position [Figs. 2(d) and 2(h)], in the gold-carbon case, two carbon peaks are observed with a blueshifted tail, indicative of the presence of fast gold ions. At the same position in the gold-helium-carbon case, no tail is observed with almost symmetric carbon peaks, indicative of a pure carbon plasma with a trace of helium.

From similar fits at various positions along the space axis, the temperature (ion and electron) and species fraction profile can be inferred (Fig. 3). Figures 3(a) and 3(b) show the ion species fraction for the two cases, where the transition from a sharp separation of the two fluids by a narrow mixing layer when ambient He is added to a uniformly hot mixed plasma in the vacuum case is clear. In the Au-C case, gold is present throughout the field of view, at an atomic fraction ranging from 5×10^{-2}, 200-μm away from the gold wall to $\sim 10^{-3}$, 300-μm away from the carbon puck. In the Au-He-C case, gold is only present in the first 300 μm from the gold wall, along with helium at about a 50/50 ratio.
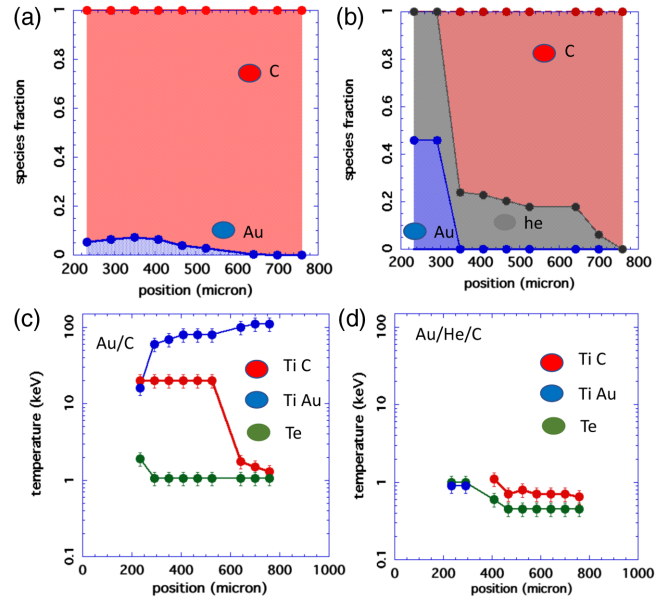

FIG. 3. Zero is the initial position of the gold ring, 1000 is the initial position of the carbon puck for all four plots. (a) species fraction for the gold-carbon case as a function of space. (b) Species fraction for the gold-helium-carbon case as a function of space. (c) Temperature (ion and electron) of the gold-carbon case as a function of space. (d) Temperature (ion and electron) of the gold-helium-carbon case as a function of space.

From 350 μm to the carbon puck, only carbon and helium are present, with a helium fraction ranging from 0.5 to about zero next to the carbon puck. Figures 3(c) and 3(d) show the temperature profile for the two cases. In the Au-C case, the ion temperature of the carbon is ~ 20 keV, where the gold species fraction is above 10^{-3}, while it stays below 1 keV everywhere when ambient He is added. Very close to the carbon puck, the carbon temperature is similar in both cases, around 1 keV, as the ablation physics is dominated by laser absorption.

Time resolved data (the scattered signal is imaged onto a optical streak camera) over a 50-μm cube volume at the 400-μm spatial position are shown in Fig. 4 for the Au-C case using the same laser drive (300 J per laser beam). The Thomson probe was on for 1 ns, starting 300 ps after the beginning of the main laser driver. The flow velocities of the two species decrease in time as the ion temperature of the two species increases, implying a transfer from the kinetic energy of the counterstreaming flows into thermal energy through Coulomb collisions [8]. Time and spatially resolved data are consistent (spatial data are taken at 1 ns for 300 ps). The carbon ion temperature is already at ~ 10 keV at 0.9 ns. The ion concentration of the two species is also measured as a function of time. At 300 ps, the gold and carbon are already mixed, which explains the high gold ion temperature (~ 20 keV). By 600 ps, the gold starts to push the carbon away from the probed zone, leading to a decrease in the carbon ion density. At all times, the plasma
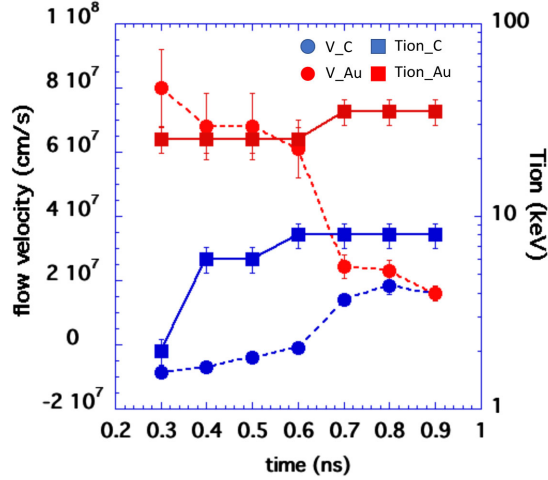
FIG. 4. The gold-carbon case. Data were taken 400 m from the Au surface. Ion temperature and flow velocities as a function of time.

is mostly composed of carbon ions with a small fraction (<1%) of gold ions, similar to the late-time spatially resolved data at this probed position.

The large differences in ion temperature reached for the two cases (tens of keV for the Au-C case, ~ 1 keV for the Au-He-C case), in mix layer width and composition, can be explained by the strong slowdown of the front of a plasma expansion in vacuum in the presence of a low-density ambient plasma. For the Au-C case, the early laser driven expansion of the gold (and carbon) can be approximated by a self-similar isothermal expansion [9] for the electron density $N_e = N_0 \exp[-(\xi + 1)]$ and flow velocity $v_i = C_s(\xi + 1)$, where $\xi = x/C_s t$, N_0 is the critical density for a 32 deg angle of incidence, and $C_s = \sqrt{[(\gamma Z K_b T_e)/M_i]}$ is the ion sound speed [here the ion sound speed is calculated for $T_e = 1$ keV, $Z = 45$ for gold ions, cf. Fig. 4(a), $C_S \sim 1.9 \times 10^7$ cm/s]. In a self-similar description, the flow velocity increases indefinitely with time and space. This description breaks down when the Debye length equals the density scale length $C_S t$ [28] due to charge separation effects. The maximum ion front velocity is then given by [29] $v_{\text{front}} = 2C_S \ln(2\tau)$, where $\tau = \omega_{pi} t / \sqrt{2e}$, ω_{pi} being the ion plasma frequency at N_0; at 300 ps, we calculate $\tau = 7.5 \times 10^3$, which gives a peak velocity of the gold ions $v_{\text{front}} \sim 3.6 \times 10^8$ cm/s and a Mach number $M \sim 19$. The electron density at $M = 19$ following the same description is $\sim 3.5 \times 10^{13}$, well below the detection threshold of our diagnostic. Experimentally, from time resolved data, the fastest the detected gold ions have reached the Thomson volume, located 400 μm from their initial position, is 300 ps. It corresponds to a velocity of $\sim 1.3 \times 10^8$ cm/s, which is about $M = 7$ at a measured electron density of 2×10^{19} cm^{-3}, which is higher than the density inferred from the self-similar expansion at $M = 7$ ($n_e \sim 6 \times 10^{18}$). Figure 4 shows that the ion temperature

at 300 ps is already high (>2 keV), suggesting that the gold ions have already slowed down on the carbon, leading to a higher ion density.

In the gold-helium-carbon case, the ion front velocity is not limited by space charge effects but by the density of the helium at the gold-helium interface [30]. This interface is a contact discontinuity, where pressure and velocity are continuous. The laser will maintain a continuous electron temperature. Assuming fully ionized He, $Z = 45$ for Au, and $T_{\text{Au}} \sim T_{\text{He}} \sim T_e$ near the interface as measured [Fig. 3(d)], equating pressures $P = N_e(T_e + T_i/Z)$ on both sides leads to $N_e(\text{Au}) = 3/2 N_e(\text{He})$. Laser-heated helium is weakly shocked by the gold expansion, and one can finally assume for this estimate that $N_e(\text{Au}) \sim 1 \times 10^{20}$ cm^{-3}, roughly twice the initial gas density. Because 0.15 mg/cm^3 of helium is transparent for the laser, one can then assume that the self-similar expansion near the ablation front is comparable for both the helium and the vacuum case. The peak gold ion velocity, set by the helium density at the Au-He interface, would have then a Mach number $\sim M = 4$, much less than in the vacuum case.

This difference in peak velocity of the gold ions has a significant impact on their mean free path through counterstreaming carbon. The ion-ion mean free path of a supersonic flow into a counterpropagating flow scales as the fourth power of the relative velocity of the two flows [31]. From the vacuum to the helium case, the peak velocity of the gold ions decreases by a factor of 1.75, which is a factor of ~ 10 in the mean free path. From the conditions measured at 300 ps in the vacuum case (cf. Fig. 4), the relative flow velocity is $\sim 10^8$ cm/s, the ion density is $\sim 5 \times 10^{19}$ cm^{-3}, and the mean free path of a gold ion into carbon is about ~ 500 μm for the vacuum case, reduced to 50 μm with ambient helium. This is consistent with the observed thickness of the mix layer in that case. The origin of a gold-helium mix layer in a high ambient gas fill density experiment was hypothesized to be the growth of Rayleigh-Taylor instabilities at the gold-helium interface. In this experiment, the initial gas electron density is ~ 20 times less than the gas electron density used in previous experiments [13], resulting in a helium fully mixed with carbon and gold, thus not slowing down the expanding gold. In addition, RT seeds were strongly reduced by optimizing the geometry of irradiation. In addition, in the vacuum case, we can observe the presence of gold mixed with carbon over hundreds of microns, which is incompatible with RT growth rate (too early). We cannot completely rule out RT instabilities as the cause of the ~ 50-μm mix layer observed in the helium case, but the physical differences of the two systems, as well as our experimental observations, do not point to RT instabilities as the source of the observed mix.

This experiment was designed to emulate the plasma conditions of a near vacuum to low gas fill He-filled hohlraum used at the NIF. The laser intensity on the wall of the Omega target is in the same range (4×10^{14} W/cm^2)

as the intensity reached on the NIF hohlraum walls. We can now explain the surprising transition observed at the NIF when the helium density was lowered below 0.3 to 0.03 mg/cm^3. Our Omega results suggest that, at 0.3 mg/cm^3 helium fill, the plasma ablated from the hohlraum gold wall and the carbon capsule remained mostly separated while they would mixed over large scale length in the near vacuum case. These changes in plasma conditions with helium fill density can explain the disagreement between radiation-hydrodynamic simulations [32] and experimental data [33] observed in the near vacuum hohlraum case and the overall good agreement at 0.3 g/cm^3 [34,35].

In conclusion, we report on a direct measurement of the impact of a gas atmosphere on the collision of two laser ablated counterpropagating plasmas. Spatially and time resolved optical Thomson scattering data show that the presence of a low-density helium (0.003% of the laser critical density) limits the peak velocity of the expanding ion flows. A clear transition is observed when gas is added, from large scale ion mixing to two plasmas separated by a narrow mixing layer. This drastically changes plasma parameters throughout the system, as observed in this Letter. The strong impact of a low-density gas fill on plasma collisions should enable control of implosion in low gas fill ICF hohlraums.

[1] H. Takabe, T. N. Kato, Y. Sakawa, Y. Kuramitsu, T. Morita, T. Kadono, K. Shigemori, K. Otani, H. Nagatomo, T. Norimatsu et al., Plasma Phys. Controlled Fusion **50**, 124057 (2008).

[2] C. M. Huntington, F. Fiuza, J. S. Ross, A. B. Zylstra, R. P. Drake, D. H. Froula, G. Gregori, N. L. Kugland, C. C. Kuranz, M. C. Levy et al., Nat. Phys. **11**, 173 (2015).

[3] T. Boehly, B. Yaakobi, D. Shvarts, D. Meyerhofer, P. Audebert, J. Wang, M. Russotto, B. Boswell, R. Epstein, R. S. Craxton et al., Appl. Phys. B **50**, 165 (1990).

[4] R. L. Berger, J. R. Albritton, C. J. Randall, E. A. Williams, W. L. Kruer, A. B. Langdon, and C. J. Hanna, Phys. Fluid B Plasma Phys. **3**, 3 (1991).

[5] K. F. Al-Shboul, S. S. Harilal, S. M. Hassan, A. Hassanein, J. T. Costello, T. Yabuuchi, K. A. Tanaka, and Y. Hirooka, Phys. Plasmas **21**, 013502 (2014).

[6] Y. Hirooka, T. Oishi, H. Sato, and K. A. Tanaka, Fusion Sci. Technol. **60**, 804 (2011).

[7] P. W. Rambo and J. Denavit, Phys. Plasmas **1**, 4050 (1994).

[8] C. Chenais-Popovics, P. Renaudin, O. Rancu, F. Gilleron, J.-C. Gauthier, O. Larroche, O. Peyrusse, M. Dirksmller, P. Sondhauss, T. Missalla et al., Phys. Plasmas **4**, 190 (1997).

[9] J. Denavit, Phys. Fluids **22**, 1384 (1979).

[10] N. C. Woolsey, Y. A. Ali, R. G. Evans, R. A. D. Grundy, S. J. Pestehe, P. G. Carolan, N. J. Conway, R. O. Dendy, P. Helander, K. G. McClements et al., Phys. Plasmas **8**, 2439 (2001).

[11] L. F. Berzak Hopkins, S. Le Pape, L. Divol, N. B. Meezan, A. J. Mackinnon, D. D. Ho, O. S. Jones, S. Khan, J. L. Milovich, J. S. Ross et al., Phys. Plasmas **22**, 056318 (2015).

[12] O. S. Jones, C. J. Cerjan, M. M. Marinak, J. L. Milovich, H. F. Robey, P. T. Springer, L. R. Benedetti, D. L. Bleuel, E. J. Bond, D. K. Bradley et al., Phys. Plasmas **19**, 056315 (2012).

[13] C. K. Li, F. H. Séguin, J. A. Frenje, M. Rosenberg, R. D. Petrasso, P. A. Amendt, J. A. Koch, O. L. Landen, H. S. Park, H. F. Robey et al., Science **327**, 1231 (2010).

[14] T. R. Boehly, R. S. Craxton, T. H. Hinterman, P. A. Jaanimagi, J. H. Kelly, T. J. Kessler, R. L. Kremens, S. A. Kumpan, S. A. Letzring, R. L. McCrory et al., Fusion Technol. **26**, 722 (1994).

[15] G. Huser, C. Courtois, and M.-C. Monteil, Phys. Plasmas **16**, 032703 (2009).

[16] J. MacFarlane, J. Quant. Spectrosc. Radiat. Transfer **81**, 287 (2003).

[17] J. Katz, R. Boni, C. Sorce, R. Follett, M. J. Shoup, and D. H. Froula, Rev. Sci. Instrum. **83**, 10E349 (2012).

[18] J. Katz, J. S. Ross, C. Sorce, and D. H. Froula, J. Instrum. **8**, C12009 (2013).

[19] D. Montgomery, B. J. Albright, D. Barnak, P.-Y. Chang, J. Davies, G. Fiksel, D. Froula, J. Kline, M. MacDonald, A. Sefkow et al., Phys. Plasmas **22**, 010703 (2015).

[20] D. Froula, L. Divol, R. London, R. Berger, T. Döppner, N. Meezan, J. Ralph, J. Ross, L. Suter, and S. Glenzer, Phys. Plasmas **17**, 056302 (2010).

[21] A. J. Mackinnon, S. Shiromizu, G. Antonini, J. Auerbach, K. Haney, D. H. Froula, J. Moody, G. Gregori, C. Constantin, C. Sorce et al., Rev. Sci. Instrum. **75**, 3906 (2004).

[22] D. H. Froula, L. Divol, N. B. Meezan, S. Dixit, J. D. Moody, P. Neumayer, B. B. Pollock, J. S. Ross, and S. H. Glenzer, Phys. Rev. Lett. **98**, 085001 (2007).

[23] R. K. Follett, J. A. Delettrez, D. H. Edgell, R. J. Henchen, J. Katz, J. F. Myatt, and D. H. Froula, Rev. Sci. Instrum. **87**, 11E401 (2016).

[24] R. W. Lee, J. Nash, and Y. Ralchenko, J. Quant. Spectrosc. Radiat. Transfer **58**, 737 (1997).

[25] P. Neumayer, R. L. Berger, L. Divol, D. H. Froula, R. A. London, B. J. MacGowan, N. B. Meezan, J. S. Ross, C. Sorce, L. J. Suter et al., Phys. Rev. Lett. **100**, 105001 (2008).

[26] S. H. Glenzer, C. A. Back, K. G. Estabrook, R. Wallace, K. Baker, B. J. MacGowan, B. A. Hammel, R. E. Cid, and J. S. De Groot, Phys. Rev. Lett. **77**, 1496 (1996).

[27] Index, edited by D. H. Froula, S. H. Glenzer, N. C. Luhmann, and J. Sheffield, 2nd ed. (Academic Press, Boston, 2011).

[28] J. S. Pearlman and R. L. Morse, Phys. Rev. Lett. **40**, 1652 (1978).

[29] P. Mora, Phys. Rev. Lett. **90**, 185002 (2003).

[30] A. V. Gurevich, Sov. Phys. JETP **22**, 449 (1989).

[31] A. Decoster, P. A. Markowich, B. Perthame, and P.-A. Raviart, *Modeling of Collisions* (Elsevier, New York, 1998), Vol. 2.

[32] M. M. Marinak, G. D. Kerbel, N. A. Gentile, O. Jones, D. Munro, S. Pollaine, T. R. Dittrich, and S. W. Haan, Phys. Plasmas **8**, 2275 (2001).

[33] L. F. B. Hopkins, S. L. Pape, L. Divol, N. B. Meezan, A. J. Mackinnon, D. D. Ho, O. S. Jones, S. Khan, J. L. Milovich, J. S. Ross *et al.*, Phys. Plasmas **22**, 056318 (2015).

[34] D. T. Casey, C. A. Thomas, K. L. Baker, B. K. Spears, M. Hohenberger, S. F. Khan, R. C. Nora, C. R. Weber, D. T. Woods, O. A. Hurricane *et al.*, Phys. Plasmas **25**, 056308 (2018).

[35] L. B. Hopkins, S. LePape, L. Divol, A. Pak, E. Dewald, D. D. Ho, N. Meezan, S. Bhandarkar, L. R. Benedetti, T. Bunn *et al.*, Plasma Phys. Controlled Fusion **61**, 014023 (2019).